Initial steps toward a new method of atmospheric characterization over long baseline arrays

J. F. Dooley, M. J. Creech-Eakman

Magdalena Ridge Observatory Interferometer, New Mexico Institute of Mining and Technology

ABSTRACT

Initial data for the current and ongoing experiment to measure and possibly predict the horizontal turbulent strength, C_N^2, of the atmosphere above the Magdalena Ridge Observatory Interferometer (MROI) is presented. C_N^2 is a representation of the atmosphere's ability to transport scalars and is measured using a set of Kipp & Zonen Large Aperature Scintillometers (LAS). LAS Calibration data as well as initial test data are presented and analyzed. Correlation techniques are used to determine the optimal method of C_N^2 calculation from the first generation LAS. A 19-day test over the array site was conducted and analyzed using both Fourier and wavelet analysis and filtration. Frequency analysis showed few periodic features due to the quasi-periodic nature of the signal.

Keywords — Magdelana Ridge Observatory Interferometer (MROI), Large Aperture Scintillometer (LAS), site characterization, astronomical seeing, turbulent strength, wavelet analysis

1 INTRODUCTION

Light from astronomical bodies approaches Earth as a wavefront with uniform horizontal phase but is distorted by the atmosphere before reaching the ground with non-uniform horizontal phase; these distortions in the 'isoplanar' wavefront increase in power towards shorter wavelengths. This is known as the 'phase screen' or 'seeing' and is primarily caused by tiny humidity and temperature variations between horizontal parcels of air [4, 6], likening the atmosphere to a system of lenses with different refractive indices that deform the wavefront received at ground-based observatories. The shifted wavefront is non-uniform along the horizontal axis so that two distinct points separated by a distance, d, along the deformed wavefront will be out of phase. As d increases, this phase difference becomes more pronounced causing a non-zero optical path difference (OPD) over larger baseline arrays.

In this project we aim to address how the phase screen evolves over the long baselines of the Magdalena Ridge Observatory Interferometer (MROI) through the use of Kipp & Zonen Large Aperture Scintillometers (LAS). These LAS are specifically designed to measure the structure parameter of the refractive index of air, C_N^2, an important parameter in calculating coherence length and coherence time for the phase screen [12]. C_N^2 is a representation of the "turbulent strength" of the atmosphere or, more specifically, the ability of the atmosphere to transport scalars, such as heat, humidity and other species (e.g. dust particles or atmospheric gases)[14, 4, 7, 8]. Usually an observatory site is characterized by measuring the vertical C_N^2 towards a bright astronomical target using a Differential Image Motion Monitor (DIMM), as most observatories only care about seeing in a 'pencil beam' [11]. However with larger aperture telescopes and long baseline optical interferometers C_N^2 will also vary across the width of the baseline, causing a higher dimensionality to the seeing. This project will continuously measure the C_N^2 on a horizontal path length similar to the MROI's longest baseline ($\sim$ 350 meters) directly above the center of the interferometric array with the end goal of understanding and possibly predicting the C_N^2 for specific seasons, times of day, and certain weather conditions.

This effort will be used to support the scientific observations for the facility; for instance, with a good predictive model, one could selectively choose astronomical targets based on predicted seeing levels for a certain time of day and year, or optimize readout rates for real-time systems in different locations of the array based on typical seeing behavior. These methods could also become a way to characterize future large aperture/distributed arrays at other sites.

1.1 THE LARGE APERTURE SCINTILLOMETER

As electromagnetic radiation propagates through the atmosphere it is distorted by the atmospheric medium which leads to attenuation of the signal beam. These distortions are caused by tiny fluctuations in the refractive index between different parcels of air, known as scintillations, and depend mainly on temperature and humidity [6].

Each LAS is composed of an equal-aperture (D) transmitter and receiver which create and measure an Infrared (880 nm) beam's attenuation over a path length, L. The relationship between the measured intensity and the structure parameter of the refractive index of air (C_N^2) is described for these scintillometers in section 2.1.

1.2 CALIBRATION OF LAS

The first generation LAS (MkI) uses analog circuitry to filter out high frequency transient signals that would corrupt the data. However, the MkI scintillometers have been shown to have a pair-specific systematic error due to poor LED alignment with respect to the Fresnel lens' focal length due to manufacturing errors [13]. The LED placement was optimized in the second generation LAS (MkII) which were also implemented with digital circuitry in order to produce higher quality C_N^2 measurements.

Comparison between these models is useful for determining the unique error associated with each generation and a comprehensive study was conducted at the New Mexico Institute of Mining and Technology to estimate the errors associated with seven MkI pairs with respect to the MkII [3]. In order to optimize the findings of this study, the data from both scintillometers were filtered so that unfavorable data due to adverse weather conditions was excluded. This filtering procedure, along with the mean absolute percentage error (MAPE) regression technique was used to estimate the error for each scintillometer.

Upon MROI's acquisition of these scintillometers, another calibration test was begun using a pair that had previously been found to have $\sim 14.5\%$ error [3]. While it is not the goal of this paper to reproduce or further study this discrepancy, it is important to recognize that there is an expected error in C_N^2 measurements due to the MkI systematic errors [13, 3]

2 METHODS

The 'turbulent strength' of the atmosphere, C_N^2, is important to observatory sites as it can be used to calculate the coherence length (Fried's parameter), r_0, and coherence time (Greenwood's parameter), τ_0 [12]. Fried's parameter, which is found by integrating the average C_N^2 over a vertical path length, is the typical size of a uniform parcel of air and knowledge of a site's average r_0 can help optimize the design of telescope aperture sizes and adaptive optics [11, 12]. The coherence time, τ_0, is a measure of how fast the coherent air parcels are moving and is used to determine the speed at which data must be collected and corrected during an observation.

2.1 INTERVAL AVERAGED C_N^2

There are three ways to calculate C_N^2 from LAS data [14, 7, 8, 13]. The first uses the PU_{CN2} value which is calculated by the data logger from the LAS output signal, U_{CN2} (log of C_N^2 signal):

$$PU_{CN2} = 10^3 \cdot 10^{U_{CN2}+1.15\sigma^2_{U_{CN2}}} \approx 10^3 \cdot 10^{U_{CN2}} \tag{1}$$

The datalogger is only able to calculate the RHS approximation due to the fact that $\sigma_{U_{CN2}}$ is not available in real time (see section 2.4). U_{CN2} can be used to directly calculate C_N^2, but typical values for C_N^2 are so small that they cannot be stored to the datalogger and so PU_{CN2} is a course alternative for calculating C_N^2 (equation 2).

$$C_N^2 = PU_{CN2} \cdot 10^{-15} \tag{2}$$

When data are collected, the standard deviation of the interval averaged U_{CN2} ($\sigma_{U_{CN2}}$) has been calculated by the datalogger and can be used to estimate the C_N^2 as shown in equation 3 for the MkI.

$$C_{N,\mathrm{MkI}}^2 = 10^{U_{CN2}-12+1.15\sigma^2} \tag{3}$$

The redesigned circuitry of the MkII causes a slight change in this equation (equation 4):

$$C_{N,\mathrm{MkII}}^2 = 10^{2.5\,U_{CN2}-17+1.15\sigma^2} \tag{4}$$

The PU_{CN2} calculation is also altered in a similar way ($PU_{CN2} = 10^{-3}\,10^{\,2.5\,U_{CN2}}$, calculated by the datalogger). Finally, the fundamental theory behind scintillation measurements states that two LAS with equal aperture diameters, D, separated by a horizontal distance, L, gives

$$C_N^2 = 1.12\sigma_{\ln(I)}^2 D^{7/3} L^{-3} \tag{5}$$

Where $\sigma_{\ln(I)}$ is the dimensionless measured variance of the natural logarithm of the beam intensity (equation 6) [14, 7, 8].

$$\sigma_{\ln(I)}^2 = \ln\left(1 + \frac{\sigma_I^2}{\overline{I}}\right) \tag{6}$$

Each of these equations were used to estimate the turbulent strength (C_N^2) of the atmosphere during initial calibration and are shown in figure 1. C_N^2 has typical values between 10^{-13} and $10^{-18}\,\mathrm{m}^{-2/3}$.

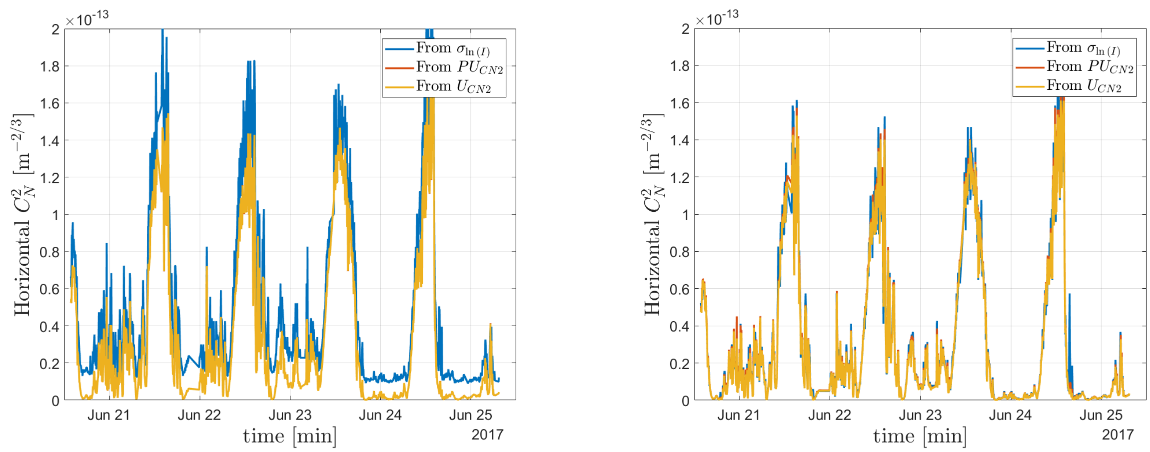

(a) MkI (1st generation) C_N^2 calculations

(b) MkII (2nd generation) C_N^2 calculations

Figure 1: Comparison of the three horizontal C_N^2 signals collected from each generation LAS during the calibration period

Equation 5 requires us to have accurate and precise (within 2 m) knowledge of the distance between the scintillometer pairs and makes the assumption that the LED is perfectly positioned at the focal point of the Fresnel lens (center of aperture). The fact that C_N^2 found using this method is noticeably different from the C_N^2 calculated from the equations 2 through 4 is most likely due to the fact that our estimated distance measurement, $L = 0.985\,\mathrm{km}$ is not measured accurately enough. Additionally, the datalogger stores the values of PU_{CN2} using the approximation in equation 2, not accounting for the non-linearity in this interval-averaged C_N^2 (the $10^{1.15\sigma_{U_{CN2}}^2}$ term). For these reasons, it is likely that equations 3 and 4 are the most accurate way of calculating the interval-averaged C_N^2.

2.2 STATISTICAL COMPARISONS

In order to get a better sense of how well these instruments and the different methods of estimating C_N^2 are related, estimates of the expectation values and covariance matrix between each of the methods were determined. For simplicity of the discussion, we will use $x_1 = C^2_{N\,(MkI)}$ and $x_2 = C^2_{N\,(MkII)}$ so that

$$E\left[C^2_{N\,(MkI)}\right] = E\left[x_1\right] = \frac{1}{N}\sum_{i=0}^{N-1} x_{1,i} \tag{7}$$

and similarly for $x_2 = C^2_{N\,(MkII)}$. By putting x_1 and x_2 in to a 2xN matrix , $\widetilde{X}$ (where x_1 and x_2 have the same length, N), we can estimate $E[x_1]$ and $E[x_2]$ with the equation

$$\hat{\mu} = \begin{bmatrix} E[x_1] \\ E[x_2] \end{bmatrix} = \frac{\widetilde{X}\mathcal{E}}{N} \tag{8}$$

where $\hat{\mu}$ is the matrix of expected values and $\mathcal{E}$ is an Nx1 matrix (column matrix) of ones. Based on this, we can estimate the covariance matrix of x_1 and x_2 using the equation

$$\widehat{COV}(x_{ij}) = \begin{bmatrix} \widehat{COV}(x_1, x_1) & \widehat{COV}(x_1, x_2) \\ \widehat{COV}(x_2, x_1) & \widehat{COV}(x_2, x_2) \end{bmatrix} = \frac{\widetilde{X}\widetilde{X}^T}{N} - \hat{\mu}\hat{\mu}^T \tag{9}$$

Using the estimates in equations 8 and 9, we can use Cholesky factorization ($\widehat{COV}(x_{ij}) = R^T R$) to create a new set of MVN (multivariate normal) distributed values that have similar features to the original data set. Mostly, were are interested in the estimated values of $\hat{\mu}$ and $\widehat{COV}(x_{ij})$, but the new set of data is helpful to determine the accuracy of these estimates (through comparison with the original data, figure 2).

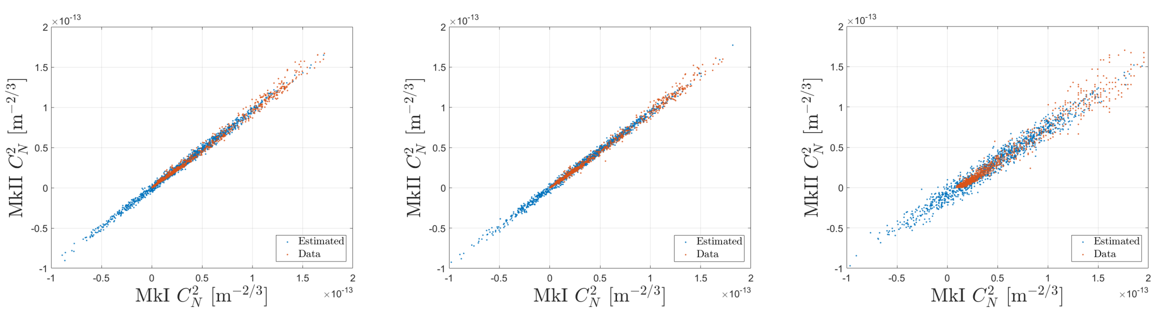

(a) PU_{CN2} method (b) U_{CN2} method (c) $\sigma_{\ln(I)}$ method

Figure 2: Data estimated from covariance and mean estimates (equations 8 and 9) for each C_N^2 calculation method

The estimated $\hat{\mu}$ and $\widehat{COV}(x_{ij})$ are shown below for each of the C_N^2 calculation methods.

$$\sigma_{\ln(I)} \text{ method (eqn. 5) :} \qquad \widehat{COV}(x_{ij}) = \begin{bmatrix} 2.197 & 1.839 \\ 1.839 & 1.590 \end{bmatrix} \cdot 10^{-27}, \qquad \hat{\mu} = \begin{bmatrix} 4.874 \\ 3.141 \end{bmatrix} \cdot 10^{-14} \tag{10}$$

$$PU_{CN2} \text{ method (eqn. 2) :} \qquad \widehat{COV}(x_{ij}) = \begin{bmatrix} 1.693 & 1.634 \\ 1.634 & 1.585 \end{bmatrix} \cdot 10^{-27}, \qquad \hat{\mu} = \begin{bmatrix} 3.293 \\ 3.124 \end{bmatrix} \cdot 10^{-14} \tag{11}$$

$$U_{CN2} \text{ method (eqns. 3 and 4) :} \qquad \widehat{COV}(x_{ij}) = \begin{bmatrix} 1.695 & 1.598 \\ 1.598 & 1.515 \end{bmatrix} \cdot 10^{-27}, \qquad \hat{\mu} = \begin{bmatrix} 3.295 \\ 3.035 \end{bmatrix} \cdot 10^{-14} \tag{12}$$

Notice that figure 2a and 2b show a much smaller variation in the data than figure 2c. This is also shown in the reported estimates (equations 10–12) with the U_{CN2} method resulting the the lowest variation between the two instruments' signals. This is in agreement with the findings by Van Kesteren and Hartogensis, 2011 [13].

All calculated and studied C_N^2 measurements throughout the rest of this document were found via the U_{CN2} method (equations 3 and 4), unless otherwise stated.

2.3 SCINTILLOMETER PLACEMENT

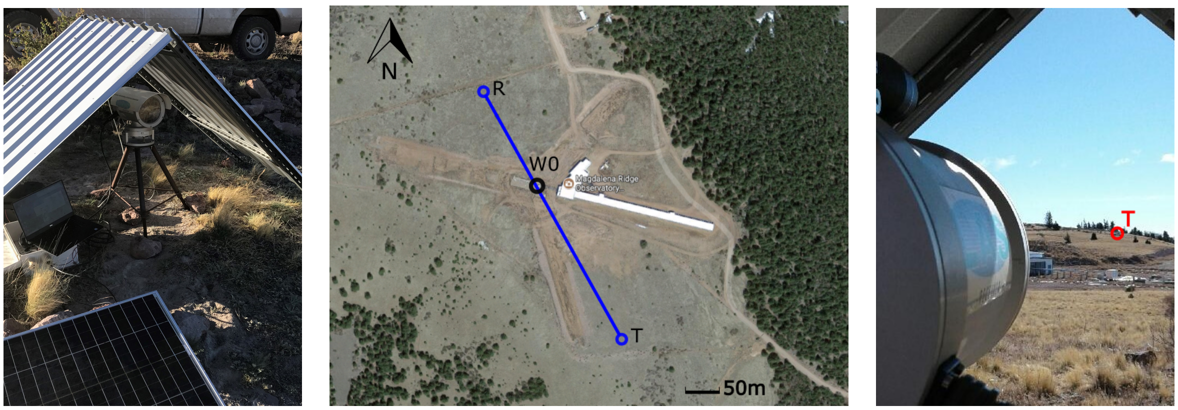

(a) (b) (c)

Figure 3: Deployment of MkI scintillometer above the MROI array site. Figure 3a: MkI receiver and protective shelter located north of the array site. Figure 3b: approximate locations of the receiver (R), transmitter (T), and horizontal beam path with respect to the center-most unit telescope location (W0). Figure 3c: Point-of-view angle from receiver to transmitter (T).

In order for the scintillometers to output meaningful C_N^2 measurements above the array site, the LAS apertures must be precisely aligned with one another and, ideally, have a horizontal beam path. Taking advantage of the unique topography around the site, a Trimble S8 total station was used to select favorable locations for the Transmitter/Receiver on hills near the array. Once the locations were selected, the total station was also used to measure the surface topography between the LAS pair (figure 4). The path-length weighting function of the LAS

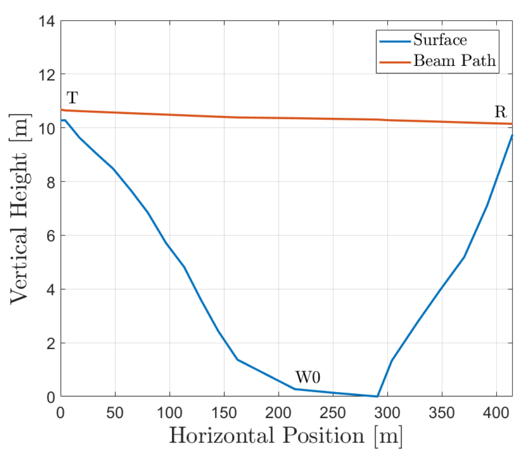

Figure 4: Horizontal and vertical locations of the first deployed MkI LAS pair with respect to center-most unit telescope (W0). Transmitter (T) and receiver (R) are located on two array-adjacent hills with the transect at a height of 10 m above the future location of the W0.

tapers to zero at the transmitter and receiver (bell-shaped curve) leading to more sensitivity towards the middle of the beam path [7, 5]. As seen in figure 4, the midpoint of the transect is nearly aligned with the center-most unit telescope (W0), giving the most sensitivity above the array.

The effective height, Z_{eff}, of the beam was found to be approximately 4.95 m using the method outlined in Hartogensis et al. (2003) for free convective conditions [5]. It should be noted that, due to the sensitivity in the C_N^2 measurements at the center of the beam path, changes in surface features at W0 (such as the installation of a 4 m enclosure) will likely change this effective height calculation.

2.4 CR1000 DATALOGGER AND POWER SUPPLY

The Campbell Scientific CR1000 dataloggers used to power the LAS and store the interval averaged C_N^2 are robust devices that can easily sample data down to a resolution of 10 ms (100 Hz). While this datalogger does have the ability to reach a maximum sampling frequency of 2000 Hz, the duty cycle is correspondingly decreased for rates higher than 100 Hz (burst data). As such, collected data at these high frequencies will register periodic, predictable gaps in data collection.

Each instrument is powered by a 12V lead-acid deep cycle marine battery which is charged daily by a large solar panel. The panel and battery are connected to a SunSaver PV system controller (SS-10L-12V). As the dataloggers do not have a built in voltage regulator, the input voltage is the same as the output voltage and so connected sensing devices are subject to any transient voltage spikes at the datalogger or power source [2]. A step-up/step-down voltage regulator (Pololu S18V20F12) was placed between the power source and datalogger in order to keep the datalogger's input/output voltage at a nominal 12 V and help protect against voltage spikes (see figure 5).

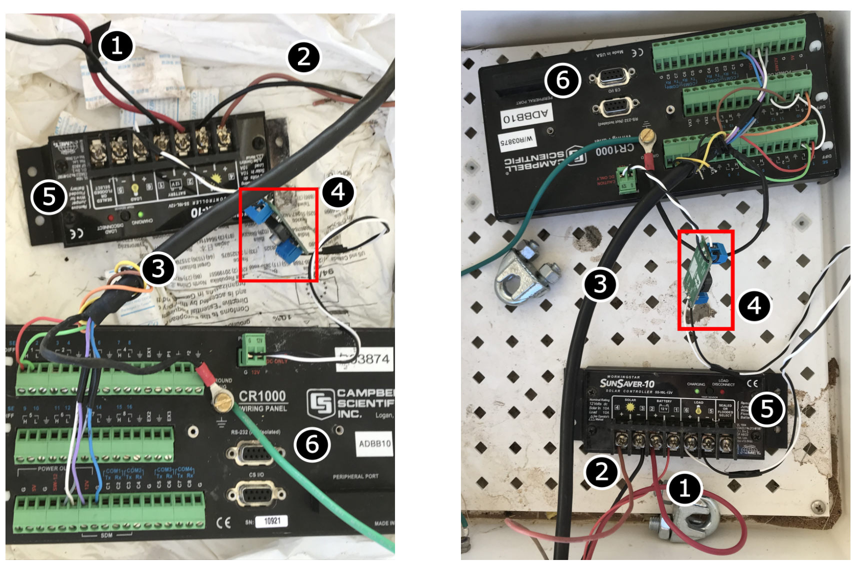

(a) Transmitter Connections (b) Reciever Connections

Figure 5: LAS transmitter/receiver power and datalogger connections. Numbered components are: **1**) lead-acid 12 V battery terminals, **2**) solar panel terminals, **3**) shielded LAS cable with hermetic connector on LAS side, **4**) Pololu 12 V step-up/step-down voltage regulator, **5**) SunSaver 10 PV controller, and **6**) Campbell Scientific CR1000 datalogger. Transmitter datalogger is connected to monitor power and temperature while the receiver datalogger requires more connections to monitor U_{CN2}, temperature, and beam intensity. Both LAS heaters are connected to power and self-regulate to maintain a constant 55° C temperature.

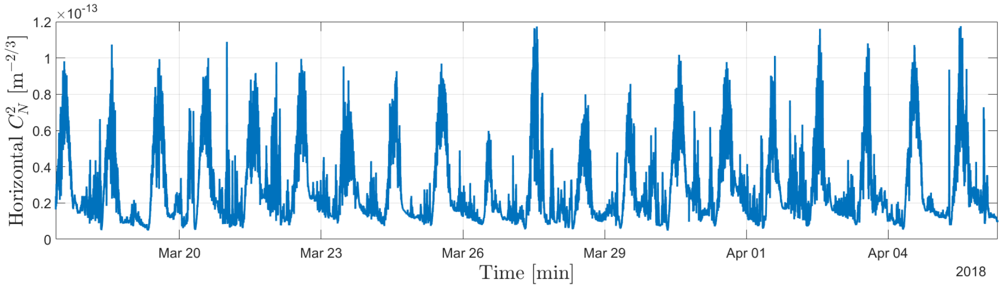

Figure 6: Full 19-day dataset (March 17 - April 5th 2018)

3 ANALYSIS

With the MkI scintillometers deployed on the ridge, a new data set over the course of 19 days was recorded and presented in figure 6. The datalogger was programmed to take measurements every second and the average U_{CN2} was calculated and stored every 5 minutes (effective sampling rate of 33 mHz). While this data is clearly periodic in nature it is also quite noisy with the signal varying a lot over the course of only a few minutes. The data was analyzed in the frequency domain and found to have a very strong peak at $f/f_s = 0$ (DC) and so the average value of the data was set to zero in an attempt to remove this offset in the spectrum. This mean adjusted data and frequency spectrum is shown in figure 7. Notice that the mean adjusted frequency spectrum still has a strong peak as it approaches $f/f_s = 0$, even after the DC offset (mean of data) is removed. Studying the frequency spectrum shown in figure 7b, it is clear that a lot of the information is contained at very low frequencies around DC, likely corresponding to the diurnal cycle ($f/f_s = 0.0035$).

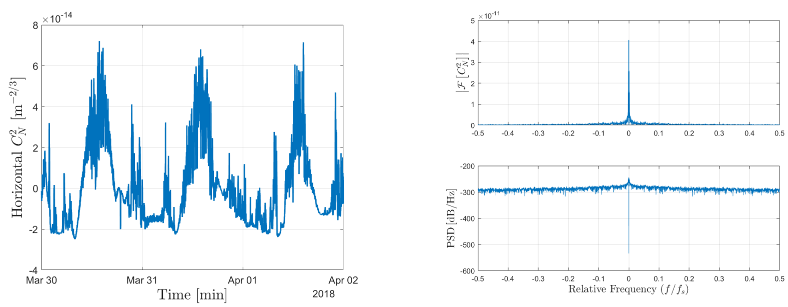

(a) **Portion** of mean adjusted signal to shown daily features

(b) Absolute value of fast fourier transform and PSD of the full, mean adjusted signal

Figure 7: Mean adjusted data and frequency spectrum

The strong peak at $f/f_s = 0$ was filtered out using a simple Butterworth filter (8th order, cutoff frequency $f_c = 0.025\, f_s$) implemented using a zero-phase digital filtering process (figure 8). This process filters the signal normally but then reverses the output and filters it again to undo any phase distortion created by the filter. The effective filter order is double the original due to this twofold filtration method.

In order to decrease the noise, the power spectral density (PSD) was estimated using the Welch method with different window sizes (figure 9). While these estimates show a large decrease in noise level, there are no obvious higher frequency contributions uncovered in the data.

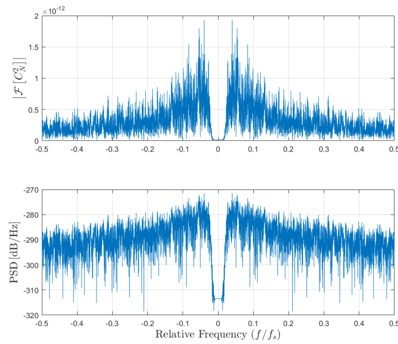

Figure 8: IIR Highpass filtered frequency spectrum of the 19-day dataset (mean adjusted)

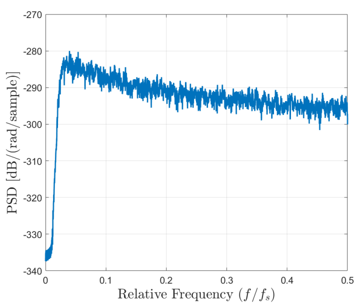

(a) Segment length = 5000

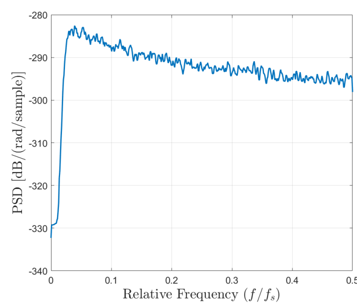

(b) Segment length = 1000

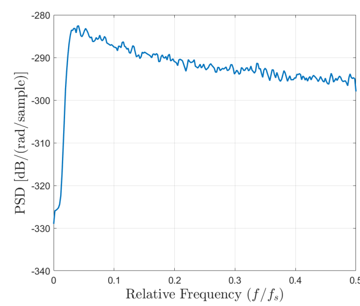

(c) Segment length = 500

Figure 9: Estimates of the one sided PSD for the highpass filtered, mean adjusted dataset

3.1 REPRESENTATIVE DAYTIME FREQUENCY ANALYSIS

In a final attempt to locate any periodic features, this data set was broken into 19 individual 24-hour periods, d_i, and each of these segments was convolved with one another in order create a representative full-day dataset, d_{rep}.

$$d_{rep} = \mathcal{F}^{-1}\left\{\mathcal{F}\left[d_1\right]\cdot\mathcal{F}\left[d_2\right]\cdot\mathcal{F}\left[d_3\right]\cdot\ldots\cdot\mathcal{F}\left[d_{18}\right]\cdot\mathcal{F}\left[d_{19}\right]\right\} \tag{13}$$

In theory, this process would average out any random signals created during a specific day while leaving behind any signals that are present in each day. Similar to the last section, d_{rep} was mean adjusted to zero and was highpass filtered to remove the strong low frequency peak (8th order Butterworth filter, $f_c = 0.025\,f_s$). Figure 10 shows d_{rep} along with its highpass filtered frequency spectrum. As expected, d_{rep} is a smoothed out representation of a single 24-hour period. The frequency domain – while still fairly noisy – does appear to have some small peaks at around $f/f_s = 0.08$ and $f/f_s = 0.12$ (see figure 11b), corresponding to periods of 12.5 min and 8.3 min. However, these peaks are only slightly higher than the noise level and the addition of more data would be the only way to see if these peaks are truly more significant than the noise floor.

The estimates shown in figure 11 are limited by the available window sizes for the Welch method. In order to improve the results, a higher sampling rate may result in a higher-quality frequency spectrum and PSD. Using shorter collection periods to exclude the diurnal frequency from the spectra may also improve these estimates. With this level of resolution, however, there does not appear to be any specific periodic features in the data.

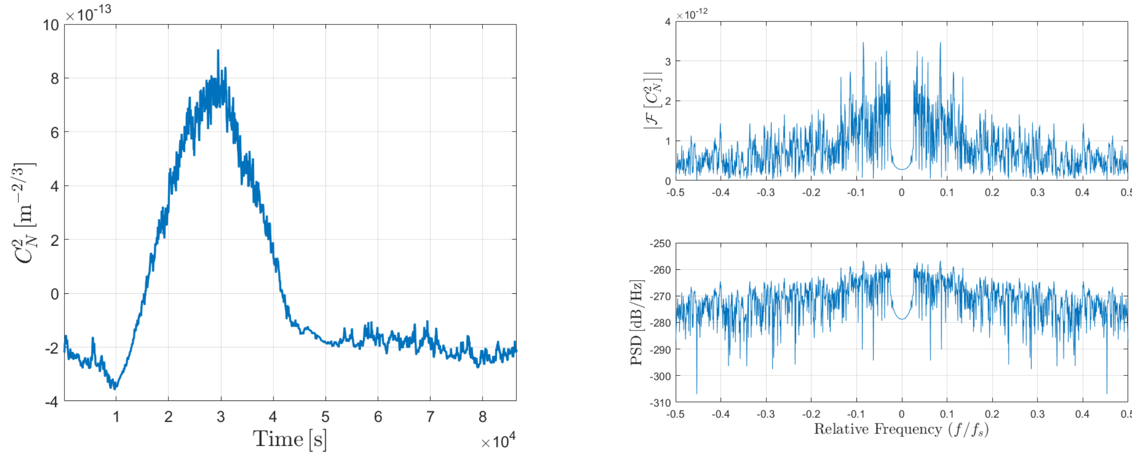

(a) representative 24-hour period, d_{rep} (mean adjusted)

(b) Frequency spectrum of d_{rep} after filtration

Figure 10

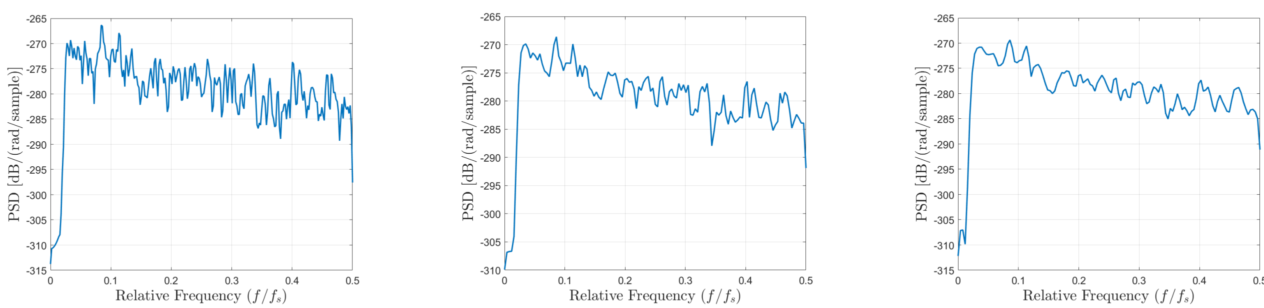

(a) Segment length = 500

(b) Segment length = 250

(c) Segment length = 175

Figure 11: Welch PSD estimates of the representative day, d_{rep}

3.2 WAVELET ANALYSIS

A relatively new method of signal processing, wavelet analysis, was also applied to these data in order to more clearly visualize the frequency contributions around DC. Wavelet analysis, specifically the continuous wavelet transform (CWT), starts with the selection of a finite energy, wave-like oscillation which is then scaled and shifted along an input signal for comparison [1, 10, 9]. While the CWT requires more time and processing power to complete than standard Fast Fourier Transform methods, the created scalograms relate the frequencies to the times they occur in the signal. Figure 12 is the CWT scalogram for the 19-day mean adjusted dataset.

The logarithmic frequency axis in figure 12 (actually only approximations or *pseudo-frequencies* [1, 9]) shows more detail around DC than the previous spectra. Notice that there is also a strong and partly intermittent band at $f \approx 0.023\,\mathrm{mHz}$ which corresponds to a period of about 12 h, the amount of daylight hours during data collection. Curiously, while this frequency contribution is strong across the entire signal, the magnitude increases and decreases every two or three days. Additionally, the data show periodic nulls at around $f \approx 0.031\,\mathrm{mHz}$ ($T \approx 9\,\mathrm{h}$). The source and explanation of these peaks and nulls will be the focus of future studies.

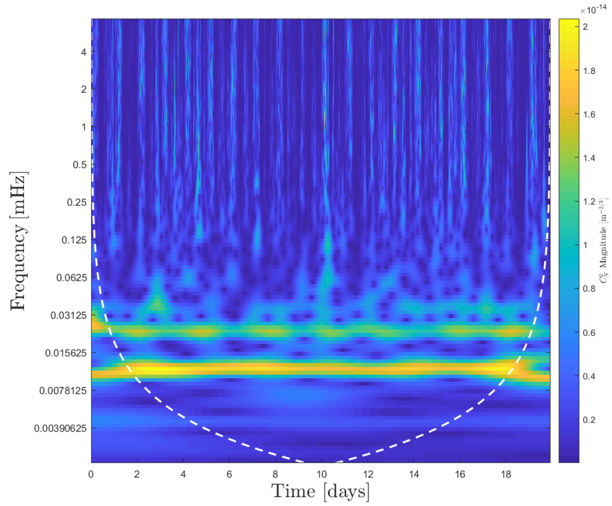

Figure 12: Scalogram of the mean adjusted dataset created using the CWT and a *morse wavelet*. The diurnal cycle ($f_s \approx 0.0116$ mHz) is now easily seen across all days due to the logarithmic frequency scale. There is also a strong frequency contribution at around $f \approx 0.023$ mHz corresponding to a period of $T \approx 12$ h, the daylight hours during data collection. The dotted white line overlaid on the scalogram represents where the edge effects begin to bias the data.

3.3 500 Hz SAMPLING

Previous seeing measurements taken at the MROI site have found that, during periods of favorable weather conditions, the average coherence time (τ_0) is between 3 and 5 ms for 500 nm light [11]. In order to study the horizontal seeing measurements at this scale, the data loggers (Campbell Scientific CR1000) were set to sample at 500 Hz. Reaching this high frequency sampling rate is difficult due to the fact that the CR1000 duty cycle must decrease for $f_s > 100$ Hz in order for the logger to complete overhead tasks and process data stored in the buffers [2]. Tests of many different scan intervals which sample at $f_s = 500$ Hz show that the maximum allowable duty cycle, without loss of information, is $\sim 66\%$. Figure 13 shows a preliminary data set which samples at $T_s = 2$ ms (500 Hz) for 40 seconds and completes overhead tasks during the remaining 20 seconds of every minute. Moving average and standard deviation procedures were used to calculate the interval averaged C_N^2 (equation 3).

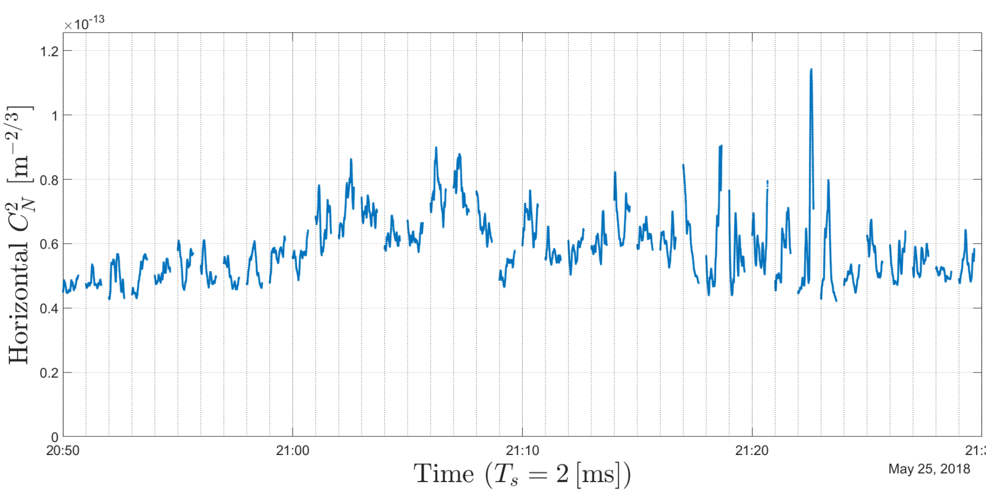

Figure 13: Horizontal C_N^2 measurements sampled at $f_s = 500$ Hz. 40 minutes of data was collected starting 40 minutes after sunset.

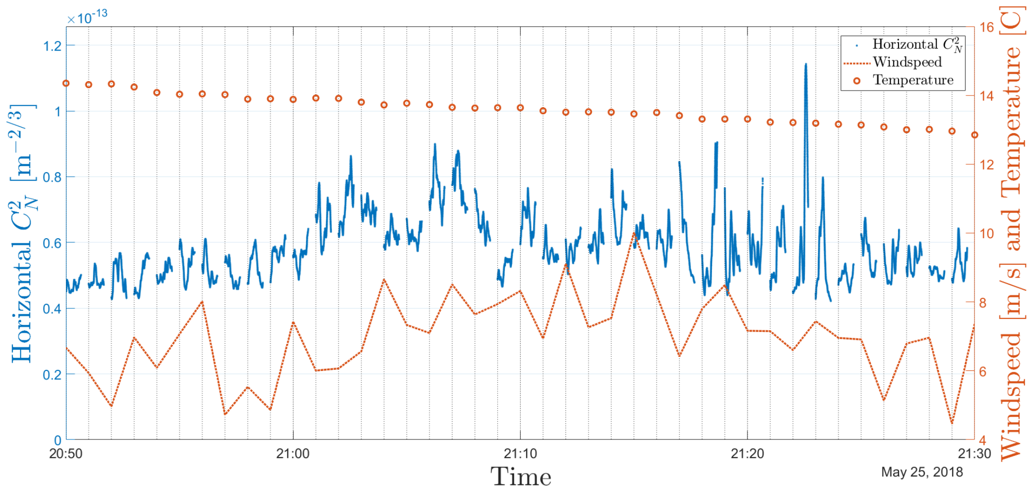

Figure 14: C_N^2 with overlaid wind speed and temperature data sampled at one minute intervals

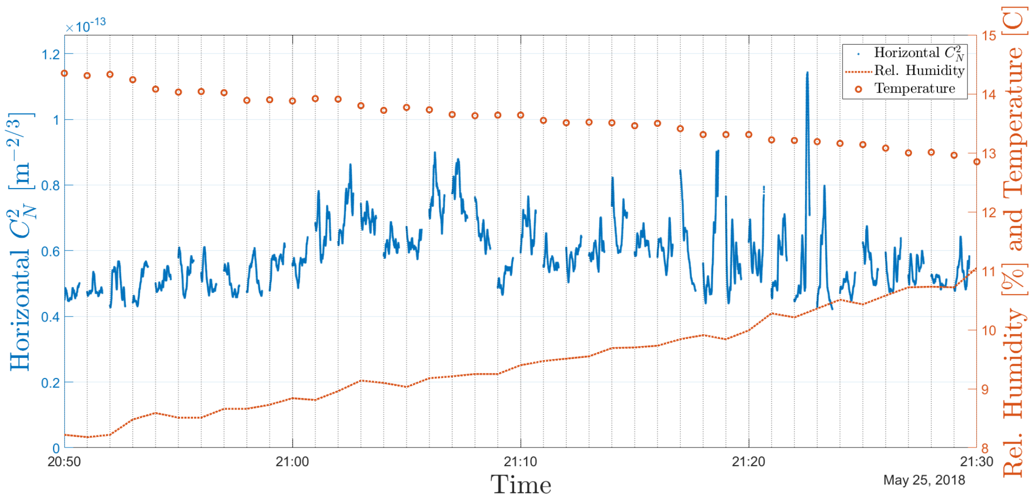

Figure 15: C_N^2 with overlaid relative humidity and temperature data sampled at one minute intervals

The 40 minute data set shown in figure 13 began 40 minutes after sunset and the C_N^2 variations are clearly visible. Due to the decreased duty cycle there is a periodic gap in the data and interpolation to fill these gaps is likely to bias the data; C_N^2 measurements can have large variations in over only a few seconds. Future code iterations will continuously sample for longer burst periods, while still meeting the processing requirements of the data logger.

Figures 14 and 15 shows the wind speed, temperature, and relative humidity overlaid with the C_N^2 measurements. In figure 15, it appears as though the C_N^2 fluctuations increase with an increase in humidity. It is unclear how the wind speed affects C_N^2 at this resolution (measured every minute).

4 DISCUSSION

The Kipp & Zonen LAS used for this project are robust and well studied instruments that are often used in hydrological studies over many terrains. Using them to classify horizontal seeing over a long-baseline array site is an exploration of the sensor and data collection limitations. While the five minute interval-averaged C_N^2 estimates analyzed in the main 19-day dataset is useful for studies in hydrology, the period between data points may be too large to create accurate and useful frequency spectra. In section 3, an exhaustive study of the Fourier transformed data showed no periodic features. While Fourier analysis is a powerful tool for time series analysis, it is fairly limiting due to the assumed periodicity in the signal. Wavelet analysis, while similar to typical frequency analysis, was found to be much more informative due to the fact that the 'pseudo-frequencies' could be matched to specific times in the data and the logarithmic scale showed much more detail towards the lower frequencies.

This is an ongoing project and future studies will be more focused on higher sampling rates over longer periods of time in order to understand more about how the turbulent strength of the atmosphere changes with different weather conditions. Knowledge of wind speed, temperature, and precipitation can be correlated to changes in the horizontal C_N^2 as a function of time. These measurements must be taken at a comparable sampling rate as the C_N^2 in order to make useful comparisons. Additionally, the signal appears to be quasi-periodic in nature and forecasting using autoregressive moving average models (ARMA or ARIMA models) can help predict changes in the horizontal C_N^2 measurements. These methods require much more data than the current 19-day set analyzed in section 3 but allow for a similar slow interval averaging rate.

It is unlikely that there will be any reoccurring trends in the data during very short bursts due to the random nature of the astronomical seeing. In addition to the fast sampled weather data, similarly timed and sampled measurements taken consistently over the coming seasons may reveal how the turbulent parameter responds to different stimuli. Additionally, with multiple MkI scintillometers at our disposal, measurements over different heights and beam path lengths can be performed in parallel.

ACKNOWLEDGEMENTS

This material is based on research sponsored by Air Force Research Laboratory (AFRL) under agreement number FA9453-15-2-0086. The U.S. Government is authorized to reproduce and distribute reprints for Governmental purposes notwithstanding any copyright notation thereon. The views and conclusions contained herein are those of the authors and should not be interpreted as necessarily representing the official policies or endorsements, either expressed or implied, of Air Force Research Laboratory (AFRL) and or the U.S. Government.

REFERENCES

[1] Paul S. Addison. *The Illustrated Wavelet Transform Handbook*. Institute of Physics Publishing, 2002.

[2] Campbell Scientific, Inc. *CR1000 Measurement and Control System (Operators Manual)*, 5/13 edition, 2010.

[3] John Chilleri, Brian Borchers, Sebastian Hendrickx-Rodriguez, and Jan Hendrickx. *Calibration procedures for large aperture scintillometers. 2016 NM WRRI Student Water Research Grant Report*. Jan 2016.

[4] Carl A. Friehe, John Larue, F.H. Champagne, and Carl Gibson. Effects of temperature and humidity fluctuations on the optical refractive index in the marine boundary layer. 65:1502–1511, 12 1975.

[5] O.K. Hartogensis, C.J. Watts, J.-C. Rodrigues, and H.A.R. De Bruin. Derivation of an effective height for scintillometers: La poza experiment in northwest mexico. *Journal of Hydrometry*, pages 915–928, Oct 2003.

[6] R.J. Hill, S.F. Clifford, and R.S. Lawrence. Refractive index and absorption fluctuations in the infrared caused by temperature, humidity, and pressure fluctuations. 70:1192–1205, Oct 1980.

[7] Kipp & Zonen, B.V. *Instruction Manual: LAS & X-LAS (Extra) Large Aperture Scintillometer*, v0307 edition, 2007.

[8] Kipp & Zonen, B.V. *Instruction Manual: LAS MkII Scintillometer*, v1207 edition, 2012.

[9] Michel Misiti, Yves Misiti, Georges Oppenheim, and Jean-Michel Poggi. *Wavelet Toolbox 4 User's Guide*. MathWorks Inc., 2015.

[10] Wai Keng Ngui, M. Salman Leong, Lim Meng Hee, and Ahmed M. Abdelrhman. Wavelet analysis: Mother wavelet selection methods. In *Advances in Manufacturing and Mechanical Engineering*, volume 393 of *Applied Mechanics and Materials*, pages 953–958. Trans Tech Publications, Nov 2013.

[11] B. O'Donovan, E.B. Seneta, J.S. Young, and D.A. Klinglesmith III. Dimmwit measurements of the spatial and temporal scale of atmospheric turbulence at COAST and MROI, 2004.

[12] A. Tokovinin. From Differential Image Motion to Seeing. *pasp*, 114:1156–1166, Oct 2002.

[13] B. Van Kesteren and O.K. Hartogensis. Analysis of the systematic errors found in the kipp & zonen large-aperture scintillometer. *Boundary-Layer Meteorology*, 138(3):493–509, Mar 2011.

[14] Ting-i Wang, G.R. Ochs, and S.F. Clifford. A saturation-resistant optical scintillometer to measure C_N^2. *J. Opt. Soc. Am.*, 68(3):334–338, Mar 1978.